C: Energy Conversion and Storage; Energy and Charge Transport

Cobalt Doping as a Pathway to Stabilize the Solid-State Conversion Chemistry of Manganese Oxide Anodes in Li-Ion Batteries

Alessandro Palmieri, Sajad Yazdani, Raana Kashfi-Sadabad, Stavros G. Karakalos, Michael Thompson Pettes, and William Earl Mustain

J. Phys. Chem. C, **Just Accepted Manuscript** • DOI: 10.1021/acs.jpcc.8b00403 • Publication Date (Web): 16 Mar 2018

Cobalt Doping as a Pathway to Stabilize the Solid-State Conversion Chemistry of Manganese Oxide Anodes in Li-Ion Batteries

Alessandro Palmieri[b], Sajad Yazdani[c], Raana Kashfi-Sadabad[d], Stavros G. Karakalos[e],

Michael T. Pettes[c] and William E. Mustain[a]*

[a] *Department of Chemical Engineering, Swearingen Engineering Center, University of South Carolina, Columbia, SC 29208*

[b] *Department of Chemical & Biomolecular Engineering, University of Connecticut, Storrs, CT 06269-3222*

[c] *Department of Mechanical Engineering, University of Connecticut, Storrs, CT 06269-3139*

[d] *Institute of Material Science, University of Connecticut, Storrs, CT 06269-3136*

[e] *College of Engineering and Computing, Swearingen Engineering Center, University of South Carolina, Columbia, SC 29208*

ABSTRACT: Metal oxides have been widely studied in recent years to replace commercial graphite anodes in lithium ion batteries. Among the metal oxides, manganese oxide has high theoretical capacity, low cost and is environmentally friendly. However, many MnO materials have shown limited reaction reversibility and poor conversion kinetics. To understand why, in this paper we investigate the mechanism, kinetics and reversibility for the solid-state conversion reaction of MnO with Li^+. We definitively show, for the first time, that during repeated reaction cycles multiple reaction pathways occur that lead not only to the reformation of MnO but higher oxidation state Mn_3O_4 – which when combined with the poor intrinsic electronic conductivity of both manganese oxide species results in rapid loss in the amount of charge that can be stored in these materials. Learning this, the approach in this study was use cobalt doping to concomitantly stabilize the redox behavior of manganese (allowing for the gradual transformation of MnO to Mn_3O_4 over time) and to increase the intra-particle electronic conductivity of the active layer. The result is an active material, $Mn_{0.9}Co_{0.1}O$, that exhibits excellent charge stabilty and conversion kinetics (near 600 mAh/g at a rate of 400 mA/g), even over 100's of reaction cycles.

Introduction

Li ion batteries (LIBs) have been the dominant energy source in the portable electronic devices market since they were commercialized by Sony in the early 1990s[1], due to their high specific energy and high specific power densities[2]. Commercial Li-ion batteries utilize a graphite anode, lithium metal oxide cathode and $LiPF_6$ salt dissolved in a mixture of organic carbonates as the electrolyte. These batteries can supply up to 150 Wh/kg, which is 5 times lower than the requirement for long-range fully electric vehicles and far away from other emerging applications[3,4]. Therefore, there is the need to find alternative materials to increase Li ion battery energy and power density without sacrificing longevity and compactness.

The cathode side of the cell presents very few choices of materials that are suitable to be used in LIBs (typically $LiCoO_2$, $LiMnO_2$, $LiFeO_4$), all with a theoretical capacity lower than 300 mAh/g. This is due to the fact that the active compound must include lithium, be resistant to corrosion, and have a high reversible Nernst potential. In contrast, the anode side of the cell presents a wide variety of chemistries with theoretical capacities significantly higher than graphite that could be suitable for Li ion battery operation. In fact, several classes of materials have been proposed in recent years including pure elements/metals (Si, Ge, Sn, Sb)[5,6], as well as metal fluorides[7], nitrides[8], phosphides[9], hydrides[10] and oxides[11-13].

Among the list above, one of the most promising categories to replace graphite in the LIB anode is metal oxides, and manganese oxides in particular, due to the multiple advantages that they offer: they are relatively inexpensive, highly abundant in nature and environmentally friendly. However, not all metal oxides behave the same and Li storage can occur through 3 different mechanisms: intercalation, alloying and conversion[14]. Conversion metal oxides undergo a bond-breaking reaction with Li^+, which causes a chemical transformation from the oxide to the metallic state, following the general formula given in Equation 1:

$$M_xO_y + 2yLi + 2ye^- \leftrightarrow xM + yLi_2O \quad (1)$$

Although this is a solid-state reaction that leverages chemical transformations (where bonds are broken and formed) to store and deliver energy, the overall anode electronic conductivity can be reaction-limiting for two reasons. First, metal oxides are typically semi-conductors; therefore, their intrinsic electronic conductivity is low (10^{-8} – 10^{-3} $\Omega^{-1}cm^{-1}$). Second, the formation of the Li_2O phase is problematic. Above a few nm in size, Li_2O is not electrically conducting, which can trap the material in the metallic (charged) state, resulting in very poor reaction reversibility that would mean rapid fade in battery capacity with cycling and limited cycle life. For these reasons, raw manganese oxides have shown very poor capacity retention with deep capacity fade even after only 10 cycles of operation[15].

In order to improve MnO electrochemical kinetics and reaction reversibility, various approaches have been tried, such as creating complex high surface area nanostructures. Li et al. synthetized interconnected porous MnO nanoflakes on nickel foam, retaining 400 mAh/g over 100 cycles at 1230 mA/g[16] (approximately a 2C rate); Cui et al. have developed a radio-sputtering technique to deposit a MnO thin film on top of copper electrodes, showing 400 mAh/g at a C/20 current rate[17]. Although these nanostructures may help reaction reversibility by shortening the Li ion diffusion pathway, showing good results at low current rates, they still were not able to achieve high capacities at fast rates due to the limited electronic conductivity. To overcome the limited electrode conductivity, one popular strategy consists of pairing the MnO active material with a highly conductive matrix such as graphene oxide or carbon nanotubes (Figure S1 in the Supporting Information), which dramatically increases the inter-particle electronic conductivity[18], resulting in higher reaction reversibility and therefore higher capacity. Increasing the electrode conductivity has also been suggested to help decrease the domain size of the Li_2O + Metal phases and therefore improve the metal oxide conversion reaction reversibility[19,20] as well as providing a buffer for the volumetric expansion that occurs during lithiation/delithiation[21,22,23].

Although synthesizing metal oxide/carbon composites may be one of the best strategies to achieve stable electrochemical conversion in some metal oxide anodes, this is not sufficient for MnO because of its very poor intrinsic electronic conductivity (10^{-8} $cm^{-1}\Omega^{-1}$, one of the lowest among all metal oxides). Therefore, a more advanced strategy to increase the reaction reversibility of MnO, and metal oxides in general, is co-doping the active material in order to manipulate its intra-particle electronic conductivity[24,25]. One element with proven electrochemical synergy with Mn is Co. A relevant example has recently been reported for pseudo-capacitors[26,27], where Co can stabilize the redox behavior of manganese oxide, inhibiting anodic dissolution and improving stability over many cycles. Also, the electronic conductivity of Co-derived oxide species is higher than Mn-based oxides. Adding just 10 atomic % Co to MnO increases its intrinsic conductivity by more than an order of magnitude, as confirmed by Van Der Pauw measurements[28] (Table S1 in the Supporting Information).

However, to the best of our knowledge, no studies have been conducted either on the influence of doping on the kinetics of the MnO conversion reaction or on its reaction reversibility, leaving these as important open questions to address. In order to do so, five $Mn_xCo_{1-x}O$ /CNT materials with different percentages of Co inclusion (x = 0, 0.05, 0.1, 0.15 and 0.2) were synthesized and characterized both physically and electrochemically.

Experimental Details

The samples were prepared in two steps[18,29]. First, multiwall carbon nanotubes (MWCNTs, Sigma-Aldrich catalogue number 724769) were oxidized similar to a modified Hummers' method with a lower concentration of oxidizing agent[30,31] (details in the Supporting Information). In the second step, 90 mg of the oxidized MWCNTs were well dispersed in a 122.5 ml ethanol/DI water (50:1 volume ratio) solution for 1 hr, in order to achieve a final CNT loading of 10 wt. % for each sample. Next, 3 ml of manganese(II) acetate tetrahydrate (0.6 M in DI-water) solution was added. To achieve the desired level of Co incorporation in Mn, stoichiometric moles of Mn precursor were replaced with cobalt(II) acetate tetrahydrate. The mixture was refluxed in an oil bath at 90°C for 24 hours after adding 2.5 ml of ammonium hydroxide solution. The mixture was centrifuged and the solids were dried in vacuum at room temperature for 80 hrs. Lastly, the $Mn_xCo_{1-x}O$/CNT anode material was obtained by annealing the dried sample at 600 °C for 3 hours in an argon atmosphere.

Results and Discussion

Fig 1a shows the XRD patterns for the $Mn_xCo_{1-x}O$/CNT materials with various cobalt inclusion. The peak positions for the entire material set are reported in Table S2 of the Supporting Information. 0%, 5% and 10% samples show accurate coincidence with the reported peak position in the literature[32] for a MnO Face Centered Cubic (FCC) crystal structure, showing all of the dominant peaks at 35.7, 40.3, 58.7, 70.2 and 73.8 2θ degrees. The XRD pattern for the 15% Co impregnated material shows a slight displacement to higher angles, which indicates the presence of a second material (cobalt) that is altering the d-spacing and therefore the crystal structure of the MnO active material. There is also peak widening and what appears to be a slight disruption of the (111) peak at the higher 2θ edge, which suggests the possibility for incomplete phase separation. Regarding high Co content (20%), a dramatic change is observed; indeed, two sets of peaks are clearly present. The first set can still be ascribed to MnO, although shifted due to the introduction of Co into the FCC MnO crystal structure. The second set of peaks at 35.7, 41.4 and 60.2 2θ degrees, corresponds to the (111), (200) and (220) Miller planes of cubic CoO[33].

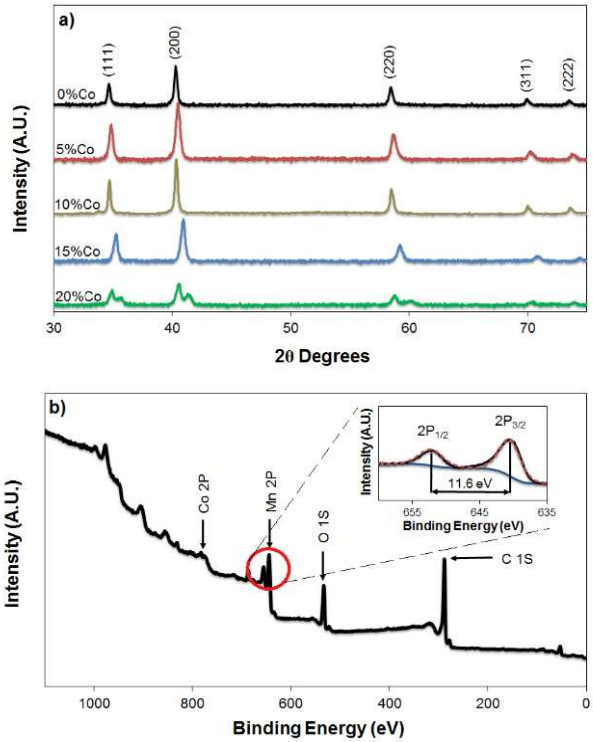

Figure 1. (a) XRD pattern for $Mn_xCo_{1-x}O$ materials with 0%, 5%, 10%, 15% and 20% Co addition. (b) XPS general survey spectrum and Mn high resolution scan for $Mn_{0.9}Co_{0.1}O$.

Fig 1b shows a typical XPS survey for $Mn_{0.9}Co_{0.1}O$/CNT. The results confirm the presence of Mn and Co on the active material surface in the expected atomic ratio (10%, Figure S2 in the Supporting Information). Moreover, the Mn high resolution scan contained only two peaks that correspond to the 2p(1/2) and 2p(3/2) orbital energies of MnO[34]. Peak deconvolution and the peak displacement (11.8 eV) confirms no metallic or higher oxidation states of manganese (3+, 4+) were present on the active material surface before electrochemical experiments were done.

Figure 2a shows a TEM image of $Mn_{0.9}Co_{0.1}O$ nanoparticles impregnated onto the CNT matrix. The image confirms a low loading of carbon nanotubes present in the active material and shows pseudo-spherical shape of the active material nanoparticles. The average particle size is between 25-40 nm, which is in good agreement with Scherrer equation calculations from the XRD pattern (Table S3 in the Supporting Information). Moreover, there was not a significant increase in the lattice parameter or in the particle size for $Mn_{0.85}Co_{0.15}O$ or $Mn_{0.8}Co_{0.2}O$ when compared to $Mn_{0.9}Co_{0.1}O$. In fact, the apparent "MnO" domain size decreased as Co was added at high levels, which confirmed that for higher Co content, cobalt was not doped into the FCC MnO structure but instead phase separated.

Figure 2b presents a high magnification image of the $Mn_{0.9}Co_{0.1}O$ nanoparticles where the lattice structure of the active material is clearly observed. The particle shows a d-spacing of 1.66 A° (in good agreement with XRD results) and an almost spherical shape, which has been shown to help dispersion and adhesion of metal oxide nanoparticles on carbon substrates[35]. Figures 2c-2f show the STEM mapping for carbon, manganese, oxygen and cobalt, respectively, using the exact TEM grid position as Figure 2a. The analysis shows the

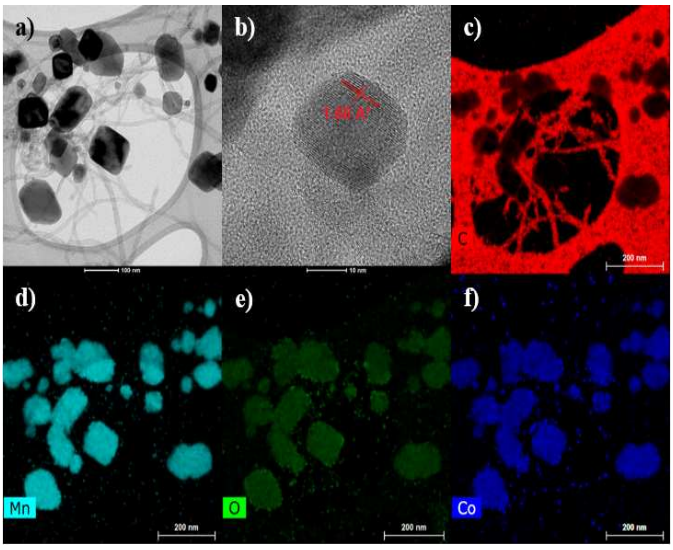

Figure 2. (a) TEM image of $Mn_{0.9}Co_{0.1}O$/CNT. (b) High magnification image of one single $Mn_{0.9}Co_{0.1}O$/CNT nanoparticle. STEM mapping images for the particles in (a) showing the elements: carbon (c), manganese (d), oxygen (e) and cobalt (f).

homogeneous presence of cobalt throughout the active material, which is greatly helped by the fact that CoO is soluble on MnO over the entire range of $Mn_xCo_{(1-x)}O$[36] compositions (0<x<1), with a complete solubility at room temperature and a maximum miscibility gap in the calculated phase diagram occurring at 242 K, due to similar Co^{2+} and Mn^{2+} cation size and rock salt structure[37]. However, some phase separation can occur on the surface under the present conditions, as shown in this and other studies[36]. Moreover, the oxygen mapping matches all of the nanoparticles, supporting the XPS result that metallic manganese is very rarely present, if at all.

The electrochemical characterization of the chemistry, kinetics and reversibility of the $Mn_xCo_{1-x}O$/CNT conversion reaction is shown in Figure 3. Figures 3a, 3b and 3c show the cyclic voltammograms for $Mn_xCo_{1-x}O$/CNT with 0%, 10% and 20% Co inclusion, respectively. These were selected because they are representative cases of no doping (3a), inclusion in the material without showing any phase separation (3b), and clear phase separation (3c). There are some common features that can be observed regardless of the cobalt concentration. In the first cathodic scan, a large peak at 0.05 V is observed, corresponding to the formation of the solid electrolyte interphase (SEI). In the $Mn_{0.8}Co_{0.2}O$ voltammogram, two peaks are present in the first polarization. The smaller peak at 0.2 V is characteristic in shape and position to SEI formation on CoO[38], further confirming phase separation at high cobalt content; the larger peak at 0.05 V can still be ascribed to SEI formation on "MnO". In subsequent cathodic scans, two peaks were always observed for all materials, the first at 0.45 V and the second at 0.3 V. In the reverse (anodic) scan, two oxidative peaks were always observed, a large peak at 1.3 V, and a smaller peak at 2.0 V.

With regards to the cathodic peaks, there is much evidence in the literature that the peak at 0.45V can be ascribed to the conversion of MnO to metallic Mn and Li_2O[39] (light brown arrow in Figure 4). The secondary peak at 0.3V is not correlated to CoO conversion[35], since it was detected in all cases, even when no cobalt was present in the active material, suggesting the possibility of a higher oxidation state of Mn being present after only one redox cycle.

The most likely higher oxidation state Mn species to be formed are Mn_3O_4 and MnO_2. There are two compelling pieces of evidence to support Mn_3O_4 as the secondary oxide phase. First, Figure S3 in the Supporting Information shows the cyclic voltammograms for Mn_3O_4 supported on CNTs. All 5 scans show a clear single cathodic peak at 0.3V and two anodic peaks, at 1.3V and 2.2V, which is consistent with what was observed in Figures 3a-c. Second, to better understand the $Mn_xCo_{1-x}O$ reaction behavior, $Mn_{0.9}Co_{0.1}O$ was cycled 300 times between 0 and 3 V vs Li/Li^+ to allow a large amount of the secondary phase to accumulate on the surface, and the resulting species were probed by XPS (Figure S4 in the Supporting Information). It was possible to deconvolute the Mn 2p region in two doublets, one that is ascribed to MnO and the other corresponding to Mn_3O_4. Moreover, the peak sets show almost the same intensity, which suggests that the two different MnO phases were present in a similar concentration (Table S4, Supporting Information), which is in good agreement with the cyclic voltammetry analysis. This is the first time in the literature that the conversion of MnO to higher oxidation states during the conversion reaction lithiation/delithiation has been definitively found, a provides new insight into the evolving understanding of the chemistry of metal oxide anode materials.

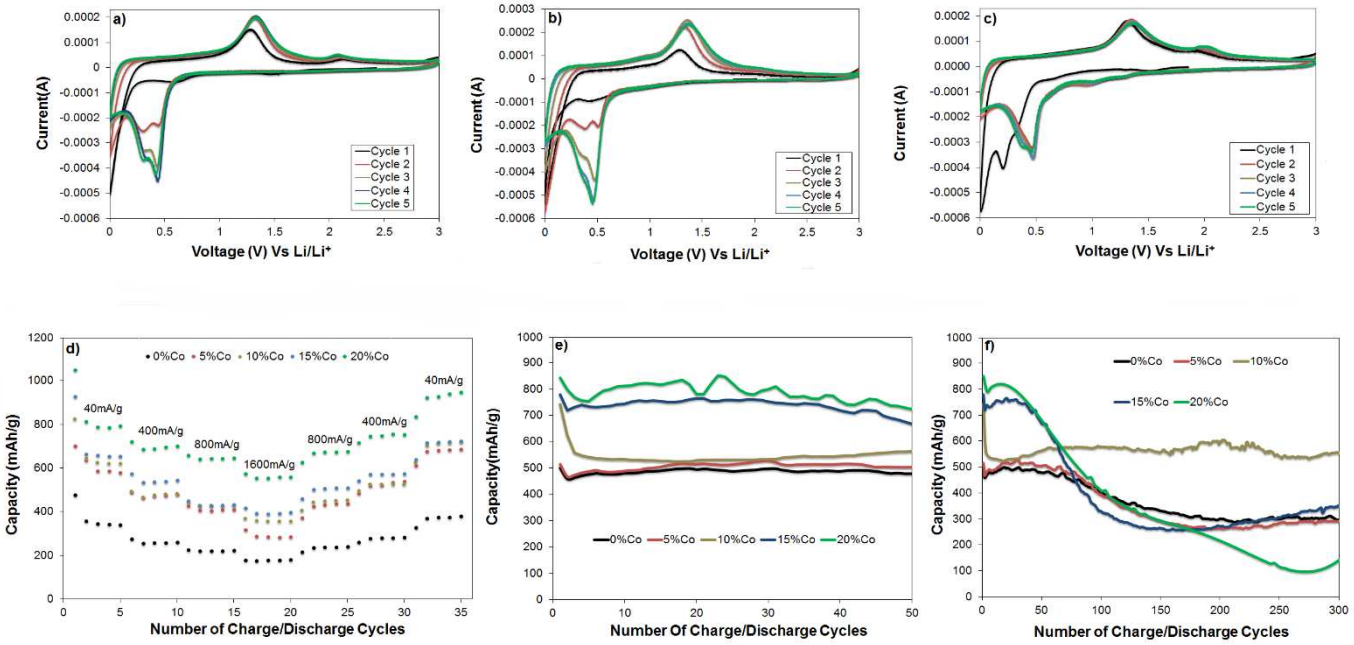

Figure 3. Cyclic voltammograms for MnO (a), $Mn_{0.9}Co_{0.1}O$ (b), and $Mn_{0.8}Co_{0.2}O$ (c), showing their redox reaction peaks. (d) Rate capability for $Mn_xCo_{1-x}O$ investigating kinetic overpotentials as a function of Co inclusion. (e) Initial charge storage ability of $Mn_xCo_{1-x}O$ at a current rate of 400 mA/g. (f) 300 charge/discharge cycles for $Mn_xCo_{1-x}O$ at a current rate of 400 mA/g, showing their long-term charge storage ability as a function of Co inclusion in MnO.

In order to account for the higher oxidation state Mn (red pathway in Figure 4) after repeated oxidation and reduction cycles, Equation 2, there are three main possibilities.

$$Mn_3O_4 + 8Li^+ + 8e^- \leftrightarrow 3Mn + 4Li_2O \quad (2)$$

First, the Mn_3O_4 that is formed contains oxygen vacancies, which has been found previously[40] in a non-battery environment. The second possibility is that MnO is converted to a higher oxidation state by reacting with oxygen species (i.e. carbonates) that are created during the formation of the solid electrolyte interphase (SEI) – the products of electrolyte decomposition. Third, it is also possible that local stoichiometry post-reduction (after charging) kinetically favors the oxidation of Mn_3O_4 (during discharge). This would also result in domains of metallic Mn post cycling, which were detected by XPS (Table S4), although not in a significant quantity as one would have expected if this was the predominant pathway.

The kinetics and reversibility of the conversion reaction was probed by carrying out charge/discharge tests at different rates for all $Mn_xCo_{1-x}O$ materials, and the results are shown in Figure 3d. First, the results generally showed a decrease in extent of reaction at higher rates, which is expected because of the increasing kinetic overpotentials the battery is experiencing with increasing reaction rate. In order to evaluate the overpotentials in-situ, the charge/discharge curves for all of the $Mn_xCo_{1-x}O$ chemistries were deconvoluted at four reaction rates (Figure S5 in the Supporting Information). Among the $Mn_xCo_{1-x}O$ materials, increasing the Co content led to lower overpotentials, with the most notable differences at high reaction rate (Table S5 in the Supporting Information). Because of the lower overpotentials, the cells were able to operate over a larger effective voltage window and thus were able to achieve a higher extent of reaction (higher capacity). In fact, MnO (0% Co doped), shows an extent of reaction of only 23.1 % (175 mAh/g) at 1600 mA/g. The $Mn_{0.95}Co_{0.05}O$, $Mn_{0.9}Co_{0.1}O$, $Mn_{0.85}Co_{0.15}O$ and $Mn_{0.8}Co_{0.2}O$ active materials were able to achieve significantly higher extents of reaction and capacities of 284, 355, 390 and 554 mAh/g (at a current rate of 1600 mA/g), respectively. The $Mn_{0.8}Co_{0.2}O$ in this work was able to achieve one of the highest capacities reported to date for any Mn anode in Lithium ion batteries at a rate of 1600 mA/g[13,16,32,39,41-45].

Knowing the overpotentials for all of the active materials as a function of the current, a Tafel slope analysis was carried out for both the reduction (lithiation) and oxidation (delithiation) reactions in order to identify the rate limiting step in the electrochemical conversion reaction. Three assumptions were made: the Mn_3O_4 reaction pathway is negligible initially because of the very few number of charge/discharge cycles that occurred during the testing; the first data point at 40 mA/g was neglected because the overpotential was too small (~10 mV) to justify its use given the inherent assumptions in the Tafel equation derivation (Equation 3); and the $Mn_{0.8}Co_{0.2}O$ was not considered because of the phase separation and consequent increasing number of reactions occurring simultaneously. The overpotentials were evaluated for both charge and discharge by taking the mid-point value between the cutoff voltage at the end of each cycle and the following data point, and the Tafel slope was evaluated for each $Mn_xCo_{1-x}O$ chemistry:

$$\eta = a + b\log i \quad (3)$$

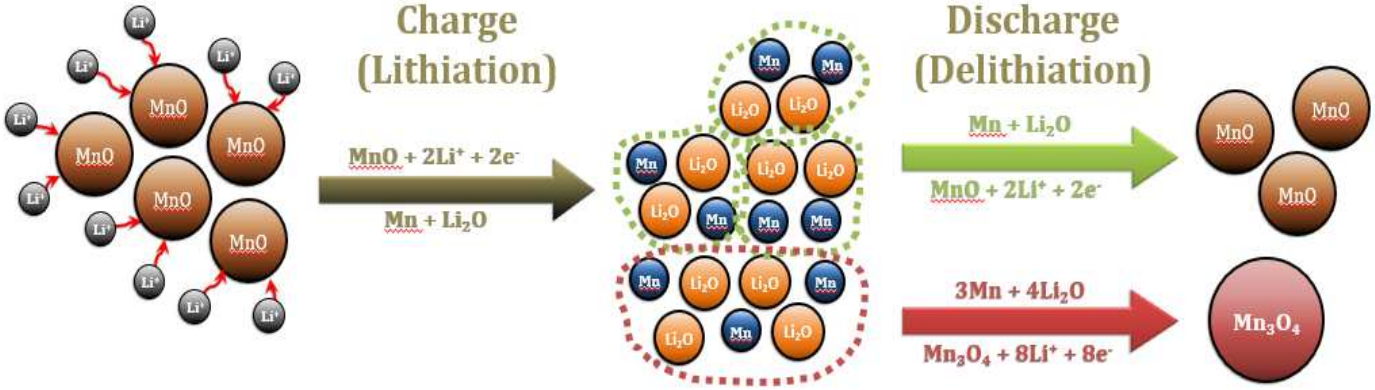

Figure 4. Proposed mechanism for MnO solid-state conversion reaction.

Where η is the overpotential at a specific current density i and b is the Tafel slope, which is defined as:

$$b = \frac{2.303RT}{F \cdot \alpha_{eff}} \quad (4)$$

Where F=96485.3 Cmol^{-1} is Faraday constant, R=8.314 J mol^{-1} K^{-1} is the ideal gas constant, T=298 K is the temperature, and α_{eff} is the effective transfer coefficient. Figure S6 in the Supporting Information shows an example of the evaluation of the Tafel slope for both forward and reverse scans for MnO. From the Tafel slope, α_{eff} was determined by Equation 4 and averaged over the four $Mn_xCo_{1-x}O$ materials in order to determine the nature of the rate determining step (RDS) using Equation 4.

$$\alpha_{eff} = \frac{\gamma}{\nu} + \rho\beta \quad (5)$$

Where γ is the number of electron transfer steps preceding the rate determining step, ν is the RDS stoichiometric coefficient, β is the transfer coefficient for a reversible reaction (which is 0.5 for most systems of interest), and ρ is a coefficient equal to 1 if the RDS is an electron transfer step or 0 if it is a chemical step. The results showed an α_{eff} of 0.54 ($\approx$ 0.5) for the reduction reaction, and an α_{eff} of 1.54 ($\approx$ 1.5) for the oxidation reaction, from which a reaction scheme proposed in Equations 6-8 can be inferred. When $\alpha_{eff} \approx$ 0.5 (Tafel slope $\approx$ 120 mV/decade) ρ=1 and γ=0, the RDS is an electrochemical step, and more specifically, the first electrochemical reaction (Equation 6), namely the formation of the MnOLi complex. During the oxidation (from Equation 8 to Equation 6), $\alpha_{eff} \approx$ 1.5 (Tafel Slope $\approx$ 40 mV/decade), $\rho = \nu = \gamma$ =1, identifying the second electrochemical step as the RDS, strongly supporting the reduction data pointing to Equation 6 as the RDS. The consistent result also suggests that the active sites for the reaction do not change whether oxidation or reduction are occurring and the primary activation hurdle lies in the MnOLi intermediate. Lastly, the individual values for the Tafel slope, and hence α_{eff}, for with varying Co content were quite consistent, showing that the underlying mechanism for the conversion of MnO is not affected by the presence of Co.

$$MnO + Li^+ + e^- \leftrightarrow MnOLi \quad (6)$$

$$MnOLi + Li^+ + e^- \leftrightarrow MnOLi_2 \quad (7)$$

$$MnOLi_2 \leftrightarrow Mn + Li_2O \quad (8)$$

To begin probing the reaction reversibility, initial charge/discharge cycles and long-term stability tests for all $Mn_xCo_{1-x}O$ active materials at 400 mA/g are reported in Figures 3e and 3f. For a limited number of redox cycles (Figure 3e), all of the $Mn_xCo_{1-x}O$ materials show good reversibility, with the exception of the phase-separated x= 0.15 and x=0.2, which experienced slight decline even within 50 cycles. When looking at extensive long-term cycling (Figure 3f), it is clearly demonstrated that the phase-separated materials are very unstable. In fact, $Mn_{0.85}Co_{0.15}O$ and $Mn_{0.8}Co_{0.2}O$ show rapid loss in reversibility (capacity fade), only realizing 347 mAh/g and 133 mAh/g, respectively, after 300 cycles at a rate of 400 mA/g. This might be due to the fact that the phase separation in the active material limits the number of surface active sites available and lengthens the path for Li ion solid state diffusion. At the other extreme, low Co inclusion had minimal impact on the reaction reversibility, showing equally poor reversibility to raw MnO. Indeed, MnO and $Mn_{0.05}Co_{0.15}O$ show a final extent of reaction after 300 cycles of only 299 and 286 mAh/g, respectively.

Interestingly, $Mn_{0.9}Co_{0.1}O$ showed the highest charge reversibility over the 300 charge/discharge cycles, and is one of the best results for a MnO-based anode to date at a rate of 400 mA/g (Table S6 in the Supporting Information). In fact, 10% Co inclusion in MnO is able to achieve excellent capacity retention, ca. 550 mAh/g for 300 cycles. Comparing charge/discharge curves at cycle 3 and 300 for the various materials (Figure S7 in the Supporting Information), only $Mn_{0.9}Co_{0.1}O$ showed low hysteresis, confirming the high reversibility of the conversion reaction in this case. This behavior appears to result from a balance between the intrinsic capacity fade of MnO with cycling and the gradual emergence of Mn_3O_4 with cycle number, which is supported below.

Features characteristic of the more gradual emergence of metallic manganese to Mn_3O_4 for $Mn_{0.9}Co_{0.1}O$ compared to the other $Mn_xCo_{1-x}O$ species can be detected from cyclic voltammograms and post-cycling XPS. In fact, both Figures 3a and 3c show clear anodic peaks at 2.2V (a fingerprint for the pres-

ence of Mn_3O_4, Figure S3), but Figure 3b only shows a very low intensity peak. Moreover, though the height and area of the two cathodic peaks during the second redox scan is comparable for the three analyzed materials, in the following redox cycles, the peak ratio changes. Only for figure 3b is the area under the cathodic peak at 0.45V substantively larger than the area under the peak at 0.35 V, confirming that the predominant species after 5 cycles is MnO for $Mn_{0.9}Co_{0.1}O$.

As further proof, the higher Co-content $Mn_xCo_{1-x}O$ materials ($Mn_{0.85}Co_{0.15}O$ and $Mn_{0.8}Co_{0.2}O$) had much higher capacities in the first 30 cycles (Figure 3e). This behavior suggests rapid transformation of MnO to higher capacity Mn_3O_4 upon cycling, which was followed by the characteristic capacity fade of Mn_3O_4, shown in Figure S8 in the Supporting Information. It should be noted that Figure S8 itself suggests that Mn_3O_4 in isolation may not be a desirable starting oxide from which to create a Li-ion battery anode.

The higher immediate capacity of the higher Co content oxides in Figure 3c-e also gives insight into which of the three mechanisms discussed previously is primarily responsible for the formation of Mn_3O_4 – reaction with the SEI. This can be concluded because of the limited oxygen that is available in the form of Li_2O after the conversion of MnO to Li_2O + Mn. Since Mn_3O_4 requires additional oxygen to form per Mn atom (Equation 2) than MnO (Equation 1) reaction of Li_2O + Mn to Mn_3O_4 would not result in an increased capacity, only orphaned metallic Mn (which was not readily observed). Also, if oxygen-vacancy laden Mn_3O_4 were formed, it could only come from the reaction of three Li_2O molecules, which would only yield six electrons, not eight, and maintain the same $2e^-$:Mn ratio as MnO – again not increasing capacity. However, it does appear that the amount of oxygen that is available to reaction from the SEI is limited, which explains why we observe the extensive (and rapid) formation of Mn_3O_4, but not higher oxidation states, like MnO_2, which we know are possible based on post-cycling XPS of anodes comprised of Mn_3O_4 initially, where almost half of the Mn becomes MnO_2 over time (Figure S9 and Table S7 in the Supporting Information). It is interesting that MnO_2 was not observed because the transformation of higher oxidation state Mn oxides to higher oxidation states during cycling is thermodynamically favored. The standard reduction potentials for the conversion reactions of MnO, Mn_3O_4 and MnO_2 were calculated to be 1.03, 1.25 and 1.70 V, respectively. Thus, the fact that MnO_2 is not detected supports the hypothesis of reactant deficiency (oxygen) in the system.

The final piece of data supporting the slow transformation of MnO to Mn_3O_4 in $Mn_{0.9}Co_{0.1}O$, is post-cycling XPS, which was carried out after 300 cycles. With pure MnO (Figure S10 in the Supporting Information), 100 % of the active material is reconverted to Mn_3O_4 at the end of the redox cycles. Recall (Table S4) that for $Mn_{0.9}Co_{0.1}O$ around half of the manganese remained as MnO, being a potential indication that the inclusion of Co limits the amount of available oxygen for MnO by forming different cobalt oxide species (CoO and Co_3O_4 in equal amounts, supported by Figure S11 and Table S8 in the Supporting Information). Therefore, it is the fight for oxygen between Mn and Co that controls the materials chemistry and gradual transformation of MnO to Mn_3O_4, a new and very interesting result. This was not observed for the higher Co-containing materials due to phase separation of CoO; thus, MnO acted as a pure, not doped, compound – rapidly forming Mn_3O_4 upon cycling. Also exciting is that by occurring over many cycles, though the all of the individual oxide phases themselves have limited stability, in operating batteries these anodes showed very good capacity retention. This shows that it is possible to decouple materials stability and reaction reversibility, or to even engineer materials with prescribed failure mechanisms that do not sacrifice performance.

Conclusion

In conclusion, a detailed study on the MnO solid state conversion reaction in Li ion batteries has been reported. All active materials showed presence of a secondary phase Mn_3O_4, which was not detect before. The degree of Co inclusion inn MnO has been shown to be a critical variable to maintain the balance between MnO intrinsic capacity fade due to particle agglomeration and Mn_3O_4 formation, by allowing gradual transformation of MnO to Mn_3O_4 during cycling. Co content optimization produced an active material able to retain stable capacity over 100's of cycles, being one of the best MnO materials reported in the literature to date. This work also opens up new pathways for investigation, including the study of other conversion reactions for low oxidation state metal oxide compounds, which could help explain some of the works in the literature where the capacity values are above the theoretical. Moreover, the presented Co inclusion approach can be extended to many other materials, being possible to find other synergistic combinations of chemistries and it might be useful for the development of new anodes for advanced, high power demanding Li ion batteries applications.

ASSOCIATED CONTENT

Supporting Information. Experimental details, charge/discharge curves at different rates and cycles, XPS details, conversion reversibility for MnO Vs MnO/Co, conductivity data, Sherrer equation data, Tafel slope data. This material is available free of charge via the Internet at http://pubs.acs.org.

AUTHOR INFORMATION

Corresponding Author

* Phone: 803-777- 4181; Email: mustainw@mailbox.sc.edu

ACKNOWLEDGMENT

This work was funded by Ford Motor Company through the Ford University Research Program, which supported the efforts of A.P and W.E.M. This work was also partially supported by the National Science Foundation under Grant No. CAREER-1553987 (M.T.P., S.Y.), the UConn Research Foundation, award number PD17-0137 (R.K.-S., S.Y.), and a GE Graduate Fellowship for Innovation (S.Y.). We are very grateful to Prof. Elena Silva, Prof. Ali Gokirmak and Lhacene Adnane for the use of the Van Der Pauw setup.

REFERENCES

(1) Nagaura, T.; Tozawa, K. Lithium Ion Rechargeable Battery, *Prog. Batteries Sol. Cells* **1990**, *9*, 209-217.

(2) Tarascon, J. M.; Armand, M. Issues and Challenges Facing Rechargeable Lithium Batteries, *Nature* **2001**, *414*, 359-367.

(3) Thackeray, M. M.; Wolverton, C.; Isaacs, E.D. Electrical Energy Storage for Transportation—Approaching the Limits of, and Going Beyond, Lithium-Ion Batteries, *Energy and Environmental Science* **2012**, *5*, 7854-7863.

(4) Zackrisson, M.; Avellan, L.; Orlenius, J. Life Cycle Assessment of Lithium-Ion Batteries for Plug-In Hybrid Electric Vehicles – Critical Issues, *Journal of Cleaner Production* **2010**, *18,* 1519-1529.

(5) Derrien, G.; Hassoun, J.; Panero, S.; Scrosati, B. Nanostructured Sn–C Composite as an Advanced Anode Material in High-Performance Lithium-Ion Batteries, *Adv. Mater*. **2007** *19*, 2336-2340.

(6) Liu, N.; Lu, Z.; Zhao, J.; McDowell, T. M.; Lee, H.W.; Zhao, W.; Cui, Y. A Pomegranate-Inspired Nanoscale Design for Large-Volume-Change Lithium Battery Anodes, *Nature Nanotechnology* **2014**, *9*, 187-192.

(7) Li, H.; Richter, G.; Maier, J. Reversible Formation and Decomposition of LiF Clusters Using Transition Metal Fluorides as Precursors and Their Application in Rechargeable Li Batteries, *Adv. Mater.* **2003**, *15,* 736-739.

(8) Snyder, Q. M.; Trebukhova, A. S.; Ravdel, B.; Clayton Wheeler, M.; DiCarlo, J.; Tripp, P. C.; DeSisto, J. W. Synthesis and Characterization of Atomic Layer Deposited Titanium Nitride Thin Films on Lithium Titanate Spinel Powder as a Lithium-Ion Battery Anode, *J. Power Sources* **2007**, *165*, 379-385.

(9) Kim, E.; Son, D.; Kim, T. G.; Cho, J.; Park, B.; Ryu, K. S.; Chang, S. H. A Mesoporous/Crystalline Composite Material Containing Tin Phosphate for Use as the Anode in Lithium-Ion Batteries, *Angew. Chem.* **2004**, *43*, 5987-5990.

(10) Oumellal, Y.; Rougier, A.; Nazri, G. A.; Tarascon, J. M.; Aymard L. Metal Hydrides for Lithium-Ion Batteries, *Nat. Mater*. **2008**, *7*, 916-921.

(11) Reddy, M. V.; Subba Rao, G. V.; Chowdari, B. V. R. Metal Oxides and Oxysalts as Anode Materials for Li Ion Batteries, *Chem. Rev.* **2013**, *113,* 5364-5457.

(12) Poizot, P.; Laruelle, S.; Grugeon, S.; Dupont L.; Tarascon J. M. Nano-Sized Transition-Metal Oxides as Negative-Electrode Materials for Lithium-Ion Batteries, *Nature* **2000**, *407*, 496-499.

(13) Wei, W.; Wang, Z.; Liu, Z.; Liu, Y.; He, L.; Chen, D.; Umar, A.; Guo L.; Li, J. Metal Oxide Hollow Nanostructures: Fabrication and Li Storage Performance *J. Power Sources* **2013**, *238*, 376-387.

(14) Palmieri, A.; Liu, Y.; He, J.; Meng, Y.; Suib, S.L.; Mustain, W.E. Metal Oxide/Reduced Graphene Oxide Anodes for Lithium-Ion Batteries, *ECS Transactions* **2015**, *66*, 47-55.

(15) Wu, M. S.; Julia Chang, P. C.; Lee, J. T.; Lin, J. C. Synthesis of Manganese Oxide Electrodes with Interconnected Nanowire Structure as an Anode Material for Rechargeable Lithium Ion Batteries, *J. Phys. Chem. B.* **2005**, *109*, 23279-23284.

(16) Li, X.; Li, D.; Qiao, L.; Wang, X.; Sun, X.; Wang, P.; He, D. Interconnected Porous MnO Nanoflakes for High-Performance Lithium Ion Battery Anodes, *J. Mater. Chem.* **2012**, *22*, 9189-9194.

(17) Cui, Z.; Guo, X.; Li, H. High Performance MnO Thin-Film Anodes Grown by Radio-Frequency Sputtering for Lithium Ion Batteries *J. Power Sources* **2013**, *244*, 731-735.

(18) Yazdani, S.; Kashfi-Sadabad, R.; Palmieri, A.; Mustain, W. E.; Pettes, M. T. Effect of Cobalt Alloying on the Electrochemical Performance of Manganese Oxide Nanoparticles Nucleated on Multiwalled Carbon Nanotubes, *Nanotechnology* **2017**, *28*, 155403.

(19) Spinner, N.; Zhang, L.; Mustain, W. E. Investigation of Metal Oxide Anode Degradation in Lithium-Ion Batteries via Identical-Location TEM, *J. Mater. Chem. A* **2014**, *2*, 1627-1630.

(20) Spinner, N.; Palmieri, A.; Beauregard, N.; Zhang, L.; Campanella, J.; Mustain, W. E. Influence of Conductivity on the Capacity Retention of NiO anodes in Li-ion batteries *J. Power Sources* **2015**, *276*, 46-53.

(21) Zhao, Y.; Li, X.; Yan, B.; Li, D.; Lawes, S.; Sun, X. Significant Impact of 2D Graphene Nanosheets on Large Volume Change Tin-Based Anodes in Lithium-Ion Batteries: A Review, *J. Power Sources* **2015**, *274*, 869-884.

(22) Reddy, A. L. M.; Shaijumon, M.; Gowda, S. R.; Ajayan, P. M. Coaxial MnO_2/Carbon Nanotube Array Electrodes for High-Performance Lithium Batteries, *Nano Lett.* **2009**, *9*, 1002-1006.

(23) Zhang, J.; Jiang, J.; Zhao, X.S Synthesis and Capacitive Properties of Manganese Oxide Nanosheets Dispersed on Functionalized Graphene Sheets, *Journal of Physical Chemistry C* **2011**, *115*, 6448-6454.

(24) Liu, Y.; Palmieri, A.; He, J.; Meng, Y.; Beauregard, N.; Suib, S. L.; Mustain, W. E. Highly Conductive In-SnO_2/RGO Nano-Heterostructures with Improved Lithium-Ion Battery Performance, *Scientific Reports* **2016**, *6*, 25860.

(25) Zhu, Y. G.; Wang, Y.; Han, Z. J.; Shi, Y.; Wong, J. I.; Huang, Z. X.; Ostrikovbcde, K.; Yang, H. Y. Catalyst Engineering for Lithium Ion Batteries: the Catalytic Role of Ge in Enhancing the Electrochemical Performance of $SnO_2(GeO_2)0.13$/G Anodes, *Nanoscale* **2014**, *6*, 15020-15028.

(26) Wei, W.; Cui, X.; Chen, W.; Ivey, D. G. Manganese Oxide-Based Materials as Electrochemical Supercapacitor Electrodes, *Chem. Soc. Rev.* **2011**, *40*, 1697-1721.

(27) Chang, J. K.; Lee, M. T.; Huang, C. H.; Tsai, W. T. Physicochemical Properties and Electrochemical Behavior of Binary Manganese–Cobalt Oxide Electrodes for Supercapacitor Applications, *Material Chemistry and Physics* **2008**, *108*, 124-131.

(28) Adnane, L.; Gokirmak, A.; Silva, H. High Temperature Hall Measurement Setup for Thin Film Characterization, *Review of Scientific Instruments* **2016**, *87*, 075117.

(29) Palmieri, A.; Kashfi-Sadabad, R.; Yazdani, S.; Pettes, M. T.; Mustain, W. E. High Performance Bi-Metallic Manganese Cobalt Oxide/Carbon Nanotube Li-ion Battery Anodes, *Electrochimica Acta* **2016**, *213*, 620-625.

(30) Hummers, W. S.; Offeman, R. E. Preparation of Graphitic Oxide, *Journal of the American Chemical Society* **1958**, *80*, 1339.

(31) Wang, H.; Cui, L. F.; Yang, Y.; Sanchez Casalongue, H.; Robinson, J. T.; Liang, Y.; Cui, Y.; Dai, H. Mn_3O_4–Graphene Hybrid as a High-Capacity Anode Material for Lithium Ion Batteries, *Journal of The American Chemical Society,* **2010**, *132*, 13978-13980.

(32) Liu, J.; Pan, Q. MnO/C Nanocomposites as High Capacity Anode Materials for Li-Ion Batteries, *Electrochemical and Solid-State Letters* **2010**, 13, A139-A142.

(33) Peng, C.; Chen, B.; Qin, Y.; Yang, S.; Li, C.; Zuo, Y.; Liu, S.; Yang, J. Facile Ultrasonic Synthesis of CoO Quantum Dot/Graphene Nanosheet Composites with High Lithium Storage Capacity, *AcsNano* **2012**, *6*, 1074-1081.

(34) Dubal, D. P.; Dhawale, D. S.; Salunke, R. R.; Lokhande, C. D. A Novel Chemical Synthesis of Mn_3O_4 Thin Film and its Stepwise Conversion into Birnessite MnO_2 during Super Capacitive Studies, *Journal of Electroanalytical Chemistry* **2010**, *647*, 60-65.

(35) Zhu, X. J.; Hu, J.; Dai, H. L.; Ding, L.; Jiang, L Reduced Graphene Oxide and Nanosheet-Based Nickel Oxide Microsphere Composite as an Anode Material for Lithium Ion Battery, *Electrochimica Acta* **2012**, *64*, 23-28.

(36) Langell, M. A.; Gevrey, F.; Nydegger, M. W.; Surface Composition of $Mn_xCo_{(1-x)}O$ Solid Solutions by X-Ray Photoelectron and Auger Spectroscopies, *Applied Surface Science*, **2000**, *153*, 114-127.

(37) Bergman, B.; Agren, J. Thermodynimic Assessment of the System CoO-MnO, *Journal of the American Ceramic Society* **1986**, *69*, 877-81.

(38) Kim, J. C.; Hwang, I.S.; Seo, S. D.; Kim, D. W. Nanocomposite Li-Ion Battery Anodes Consisting of Multiwalled Carbon Nanotubes that Anchor CoO Nanoparticles, *Material Letters* **2013**, *104*, 13-16.

(39) Sun, Y.; Hu, X.; Luo, W.; Xia, F.; Huang, Y. Reconstruction of Conformal Nanoscale MnO on Graphene as a High-Capacity and Long-Life Anode Material for Lithium Ion Batteries, *Advanced Functional Materials* **2013**, *23*, 2436-2444.

(40) Durmus, Z.; Baykal, A.; Kavas, H.; Sozeri, H. Preparation and Characterization of Polyaniline (PANI)–Mn_3O_4 Nanocomposite, *Physica B* **2011**, *406*, 1114-1120.

(41) Zhong, Y.; Zhang, B.; Luo, S.; Wen W.; Li H. Investigation on Porous MnO Microsphere Anode for Lithium Ion Batteries, *Journal of Power Sources* **2011**, *196*, 6802-6808.

(42) Mai, Y. J.; Zhang, D.; Qiao, Y. Q.; Gu, C. D.; Wang X. L.; Tu, J. P. MnO/Reduced Graphene Oxide Sheet Hybrid as an Anode for Li-Ion Batteries with Enhanced Lithium Storage Performance, *Journal of Power Sources* **2012** *216*, 201-207.

(43) Xu, G. L..; Xu, Y. F..; Sun, H.; Fu, F.; Zheng, X. M.; Huang, L.; Li, J. T.; Yang, S. H.; Sun, S. G. Facile Synthesis of Porous MnO/C Nanotubes as a High Capacity Anode Material for Lithium Ion Batteries, *Chemical Communications* **68**, *2012*, 8502-8504.

(44) Zhong, K.; Xia, X.; Zhang, B.; Li, H.; Wang, Z.; Chen, L. MnO Powder as Anode Active Materials for Lithium Ion Batteries, *Journal of Power Sources* **2010**, *195*, 3300-3308.

(45) Ji, L.; Zhang, X. Manganese Oxide Nanoparticle-Loaded Porous Carbon Nanofibers as Anode Materials for High-Performance Lithium-Ion Batteries, *Electrochemistry Communications* **2009**, 11, 795-798.

TOC Graphic

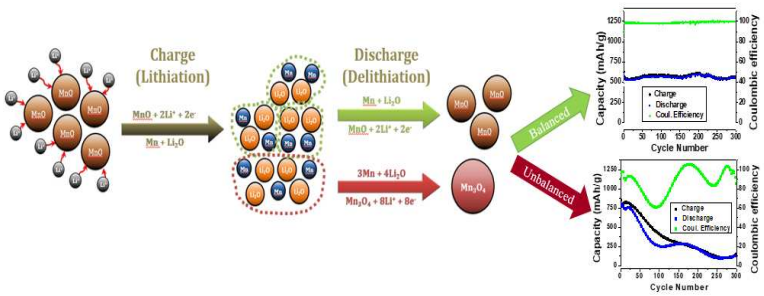
Charge
(Lithiation)
Discharge
(Delithiation)
Balanced
Unbalanced
Capacity (mAh/g)
Coulombic efficiency
Cycle Number
Charge
Discharge
Coul. Efficiency